Supporting Information to

Measuring Local Viscosities near Plasma Membranes of Living Cells with Photonic Force Microscopy

Felix Jünger,[†] Felix Kohler,[†] Andreas Meinel,[†] Tim Meyer,[‡] Roland Nitschke,[§] Birgit Erhard,[†] and Alexander Rohrbach,[†]*

[†]Laboratory for Bio- and Nano-Photonics, Department of Microsystems Engineering, University of Freiburg, Germany

[‡]Macromolecular Modelling Group, Institute of Chemistry and Biochemistry, Freie Universität Berlin, Germany

[§]Life Imaging Center (LIC) and Center for Biological Systems Analysis (ZBSA), University of Freiburg, Germany

[*]Correspondence: rohrbach@imtek.de

Estimation of the effect of the membrane curvature on the distance-dependent viscous drag

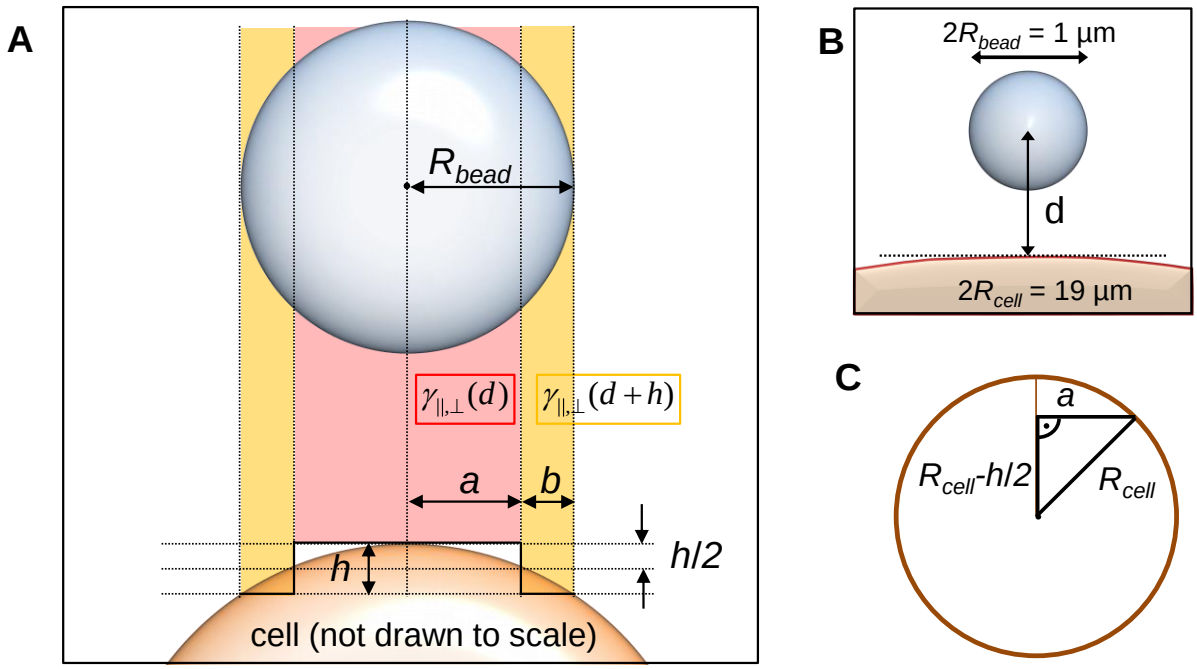

FIGURE S1 Estimated effect of the cell's curvature on the viscous drag $\gamma(d)$ close to interfaces. (A) The curvature is modeled by a stepped function with heights h and step widths a and $b = R-a$, respectively. This leads to different distances of the projected bead center to the curved surface, indicated by the red and yellow shaded regions. (B) Sketch of the actual geometry, cell and bead are drawn to scale. (C) The step height h defines the step width a with regard to the cell's radius of curvature R_{cell}.

Although the cell's radius of curvature is large compared to the bead radius, the cell membrane is not perfectly flat but exhibits a certain, albeit marginal, curvature. Here, an estimation of the effect of the curvature on the measured distance-dependent viscous drag is made. In a very simple approach, the curved cell membrane is approximated by a stepped function consisting of two steps with widths a and $b = R-a$, respectively, separated by a vertical distance h, as depicted in Fig. S1 *A*. For better visibility, the sketch in Fig. S1 *A* is not drawn to scale, a properly scaled sketch is shown in Figure S1 *B* with R_{bead} = 0.5 µm and R_{cell} = 9.5 µm as deducted from Fig. 2 in the main text. The step height h and its width $2a$ are related to each other via the cell's radius of curvature R_{cell} and can be calculated by the Pythagorean theorem $(R_{cell}-h)^2+a^2=R_{cell}^{\ 2}$, see Fig. S1 *C*. If the step is chosen to intersect the circular arc representing the cell membrane at its half height $h/2$, it immediately follows that a = 354 nm and h = 12.5 nm. This leads to the approach of superposed distances weighted by the geometrical overlap (projection) of the bead diameter with the cell surface. In terms of the spatially varying viscous drag $\gamma(d)$, the measured viscous drag has to be considered as an average of different $\gamma(d')$ corresponding to superposed distances d' between bead center and surface, each weighted by the part of the bead that sees the respective distance d'.

In our step-like approximation, the relation for the averaged $\bar{\gamma}_{\parallel,\perp}$ reads as follows:

$$\bar{\gamma}_{\parallel,\perp} = \frac{a}{R} \cdot \gamma_{\parallel,\perp}(d) + \frac{b}{R} \cdot \gamma_{\parallel,\perp}(d+h) \tag{S1}$$

The weighting factors a/R and b/R = 1-a/R correspond to the ratio of twice the surface of a spherical cap with height b ($A_{cap} = 2\pi Rb$) and the surface of the remaining sphere ($A_{rest} = 4\pi R^2 - 2A_{cap}$):

$$\frac{2A_{cap}}{A_{sphere}} = \frac{4\pi Rb}{4\pi R^2} = \frac{b}{R} \qquad \text{and} \qquad \frac{A_{rest}}{A_{sphere}} = \frac{4\pi R^2 - 4\pi Rb}{4\pi R^2} = \frac{R-b}{R} = \frac{a}{R} \tag{S2}$$

The bead fluctuations $\sigma_{\parallel,\perp}$ = 9.5 nm, which are only 1 % of the bead's diameter, are neglected in this calculation.

In the following, sample curves $\bar{\gamma}_{\parallel,\perp}(d)$ that are corrected according to Eq. S1 are presented and the deviation from the uncorrected curves is discussed. In Fig. S2 *A*, theoretical curves $\gamma_{\parallel,\perp}(d)$ according to Happel's and Brenner's formulas (see main text) are shown together with the corrected curves $\bar{\gamma}_{\parallel,\perp}(d)$ accounting for the geometrical circumstances as shown above. The same analysis is performed for $\gamma_{\parallel,\perp}(d)$ of a 1 µm bead close to a HT29 cell in Fig. S2 *B*. The curves were modeled according to Eq. 2 in the main text with the parameters obtained in the results section, i.e., $\gamma_{0\perp} = 6.23 \times \gamma_\infty$ and $\Lambda_\perp = 0.45$µm in perpendicular direction (green data) and $\gamma_{0\parallel} = 2.80 \times \gamma_\infty$ and $\Lambda_\parallel = 0.28$ µm parallel to the interface (red data).

The original curves $\gamma_{\parallel,\perp}(d)$ (solid lines) and the curves $\bar{\gamma}_{\parallel,\perp}(d)$ (dotted lines) corrected for the curvature of the interface can hardly be separated in the left part of Fig. S2, indicating that the effect of the curvature on the measured $\gamma_{\parallel,\perp}(d)$ is small. The insets with numbers 1 and 2 show magnifications of both curves close to the contact point at $d = R$, where the small deviation of both curves becomes apparent. To quantitatively estimate this effect, the $\gamma_{\parallel,\perp}(d = R)$ values and $\bar{\gamma}_{\parallel,\perp}(d = R)$ values are given in the figure insets together with the deviation Δ of these numbers in percent. It can be seen that the deviation in the given geometry is in the range of 0.5% for the HT29 cell model curve and 2.5% for the stiff glass interface. Due to the fact that $\gamma_\perp(d)$ diverges for $d \to R$ in the latter case, a mathematical estimation for Δ is only available for the parallel data.

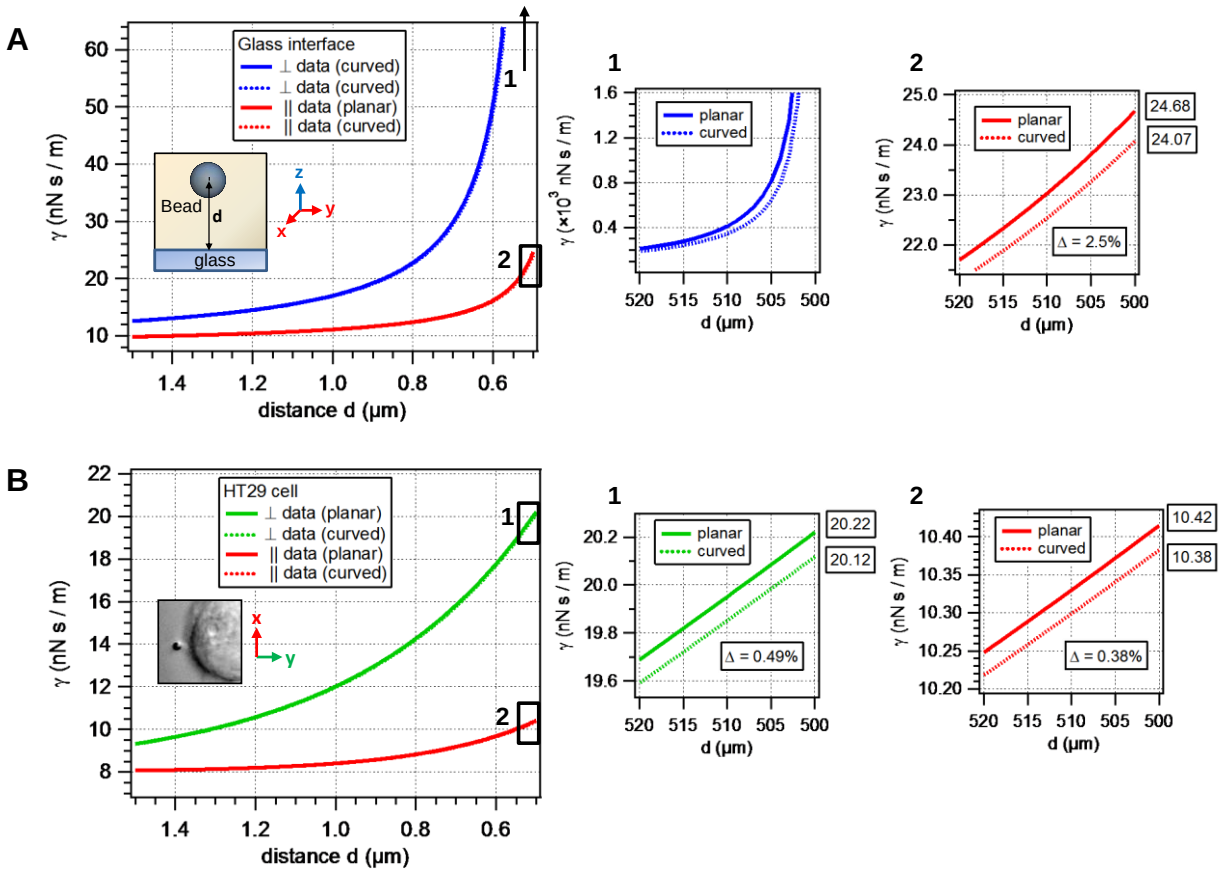

FIGURE S2 Distance-dependent viscous drag $\gamma(d)$ close to a flat (solid lines) and a curved surface (dotted lines). Both curves can hardly be separated, in the insets showing the last 20 nm before contact (d=R) the deviation of both curves of only 0.38% - 2.5% becomes apparent. (A) Case of a bead approaching a stiff planar wall according to Happel's and Brenner's formula. Blue curves correspond to the direction perpendicular to the interface, red to the parallel direction. (B) $\gamma(d)$ for a bead approaching a HT29 modeled by the parameters from the results section. Green data = perpendicular, red = parallel direction. The corrected data represents our estimate for a slightly curved cell surface.

Note that due to the oversimplification of the actual geometry as discussed above, these calculations represent only an estimate of the effect of the cell's curvature rather than a mathematically exact formulation. Nevertheless, the observed order of magnitude of this effect suggests that the curvature of the cell membrane has only a minor effect on the measured viscous drag and can therefore be neglected. For the vertical cell radius of about R_{cell} = 7.5 µm, the deviation of the corrected curve would be Δ = 3.1% instead of 2.5% and, e.g., R_{cell} = 2 µm would result in Δ = 7.9% (not shown).

QPD data recording in the proximity of the cell membrane

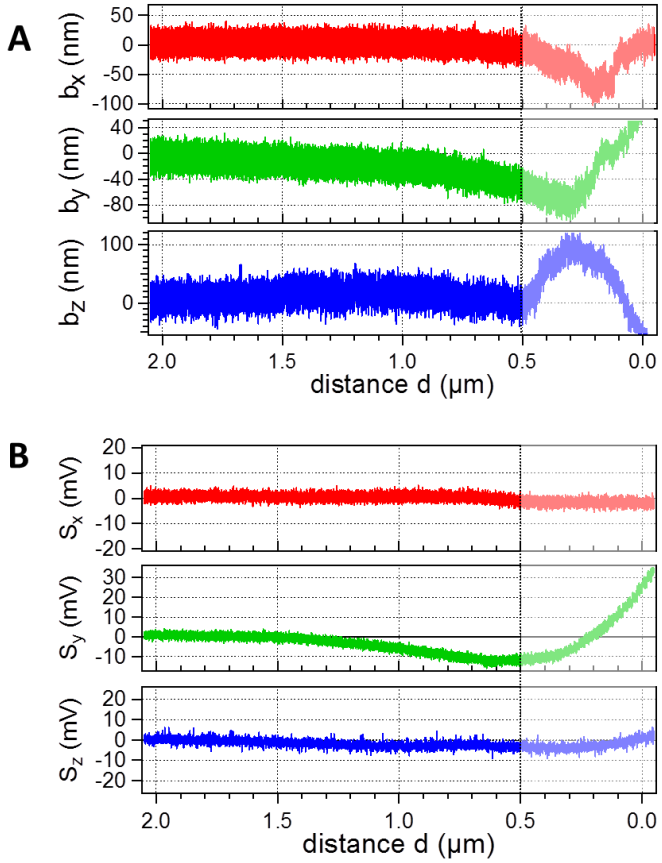

FIGURE S3 Fluctuation data close to a cell membrane. (A) Distance-dependent position trajectories $b_x(d,t)$, $b_y(d,t)$, $b_z(d,t)$ of a 1 µm sized bead approaching the membrane of a HT29 cell, calculated from the QPD data after calibration. *y* data correspond to scan direction. Bead surface and cell membrane are in contact for $d \leq R$ (masked by semi-transparent boxes). (B) QPD voltage signals of a laser focus without trapped bead are recorded upon approaching the same cell at the same site with the same parameters.

The acquisition of the QPD voltage signals and their conversion into bead position trajectories $b_x(t)$, $b_y(t)$, $b_z(t)$ via calibration is described in the main text. Figure S3 *A* shows the same data as Fig. 3 *A* together with voltage signals of an empty trap approaching the same cell on the same approach line, see Fig. S3 *B*. This control measurement allows us to estimate purely optical effects as no bead fluctuations are measured. The decrease in the *y* signal before cell contact, apparent in Figs. 3 *A* and S3 *A*, respectively, is also visible in Fig. S3 *B* and confirms the signal slope in Fig. 3 *A* (green curve) and the theoretical approach in Eq. 8. It furthermore proves that this effect must not be confused with the (small) shift of the bead trajectory's mean position due to mechanical interaction (contact) with the cell interface. The latter occurs on a much shorter length scale, namely one fluctuation width before surface contact (approximately 9 nm), compared to roughly 0.7 µm before contact deduced from Figs. 3 *A* and S3. The mechanical effect is revisited in the discussion in the main text and in the context of Fig. S5.

Computer simulations of a 1 µm bead's Brownian motion close to an interface

To study the influence of the interface on the bead's fluctuation data, Brownian dynamics (BD) simulations based on the Langevin equation were performed in addition to the experiments presented in this study. Details of the simulation algorithm can be found in (1). In brief, the bead's diffusive motion is simulated by adding a random displacement to the bead's trace $b_j(t)$ at each time step ($j = x,y,z$). The random numbers are chosen such that their temporal mean value equals zero and that the mean squared displacement $\langle (b_j(t+\tau) - b_j(t))^2 \rangle = 2D \cdot \tau$ grows linearly as expected for the free diffusion of the particle (2).

The motion of a $2R$ = 1 µm polystyrene bead in a harmonic optical trap potential with isotropic force constants κ_j = 50 pN/µm for all $j = x,y,z$ in watery solution at temperature T = 37°C was simulated. The theoretical fluctuation width according to the equipartition theorem is $\sigma_j = (kT/\kappa_j)^{0.5}$ = 9.2 nm. An obstacle in form of a rigid, infinitely large surface was introduced in y direction and subsequently approached toward the trap center in distinct steps (Δy = 4 nm for $d\text{-}R \leq 40$ nm, Δy = 10 nm for $d\text{-}R > 40$ nm). For the sake of simplicity, the distance-dependent change in viscous drag as described by Happel and Brenner was neglected in the simulation, such that $\gamma_j(d) = \gamma_\infty = 8.0 \times 10^{-9}$ Ns/m remained constant. All simulation parameters were chosen to meet the experimental conditions. The standard deviation $\sigma_y(t)$ of the bead's fluctuations in perpendicular direction was roughly 9 nm as also measured in the experiments.

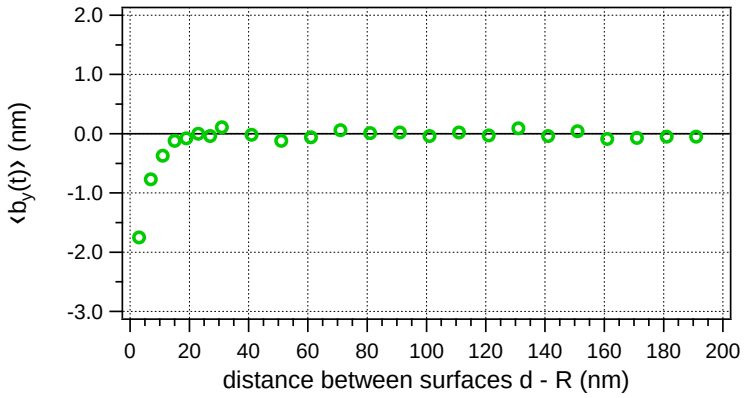

FIGURE S4 BD simulation: The mean position value $\langle b_y(t) \rangle$ of a $2R$ = 1 µm bead's diffusive motion hardly changes close to a rigid surface.

Due to short contacts of the fluctuating bead with the interface, the fluctuation volume becomes slightly asymmetric and shifts the mean value of the position histogram. Figure S4 reveals that the presence of the interface leads to a slight decrease of the mean bead's displacement $\langle b_y(t) \rangle$, which, however, only appears at distances smaller than the bead's fluctuation width, i.e., $d\text{-}R < 9$ nm. For any larger distance, the mean value remains constantly zero. This effect must not be confused with the shift of the signal that occurs due to additional light scattering at the cell, as it was discussed following Eq. 8 in the main text. Since the piezo step size in the

experiments was chosen larger than $\sigma_y(t)$ and only data points at distances d-R > 0 were considered for data analysis, this effect does not affect the data presented in this study.

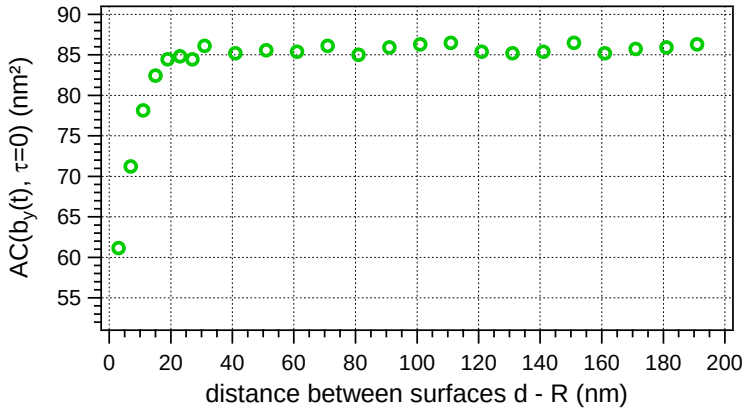

FIGURE S5 BD simulation: Distance-dependent variance $\langle b_y(t)^2 \rangle = AC(\tau=0)$ of a $2R$ = 1µm bead's diffusive motion perpendicular to a rigid surface.

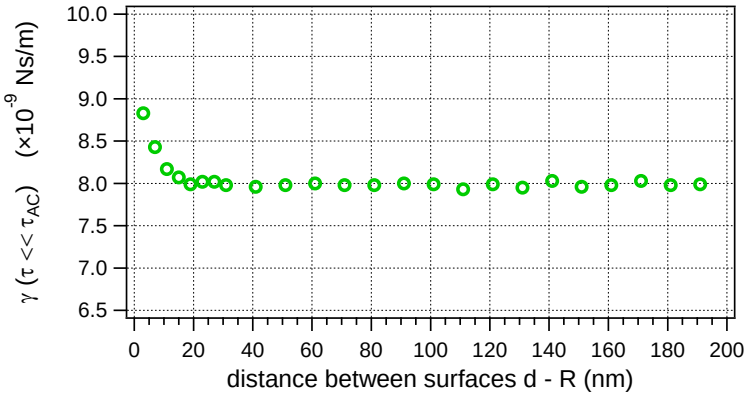

FIGURE S6 BD simulation: Distance-dependent viscous drag $\gamma_\perp(d)$ of a $2R$ = 1 µm bead's diffusive motion perpendicular to a rigid surface, calculated from the slope of the autocorrelation on time scales $\tau \leq 30$ µs. $\gamma_\perp(d)$ is increased to about $1.1 \times \gamma_\infty = 8.8 \times 10^{-9}$ Ns/m for d-R < 9 nm.

The AC(0) = $\langle b_y(t)^2 \rangle$ value, which affects the slope kT/γ used for the calculation of the viscous drag (see Eq. 4 in the main text), experiences qualitatively the same slight distortion for distances d-R < 9 nm, see Fig. S5. This immediately leads to a slight miscalculation of $\gamma_\perp(d)$, also only apparent for d-R < 9 nm, as shown in Fig. S6. As explained above, this systematic, but very small error does not impact the data presented in this study. The effects discussed here are only present in the fluctuation data perpendicular to the interface, i.e., y direction, the parallel directions however remain completely undisturbed (not shown).

In conclusion, we see that a systematic overestimation of $\gamma_\perp(d)$ of maximum 10 % occurs only at distances as small as the bead's fluctuation width, i.e., below 9 nm given the experimental parameters in this study. This is smaller than the chosen step size in our experiments and thus does not affect any data points presented in this paper.

Distance-dependent histogram width

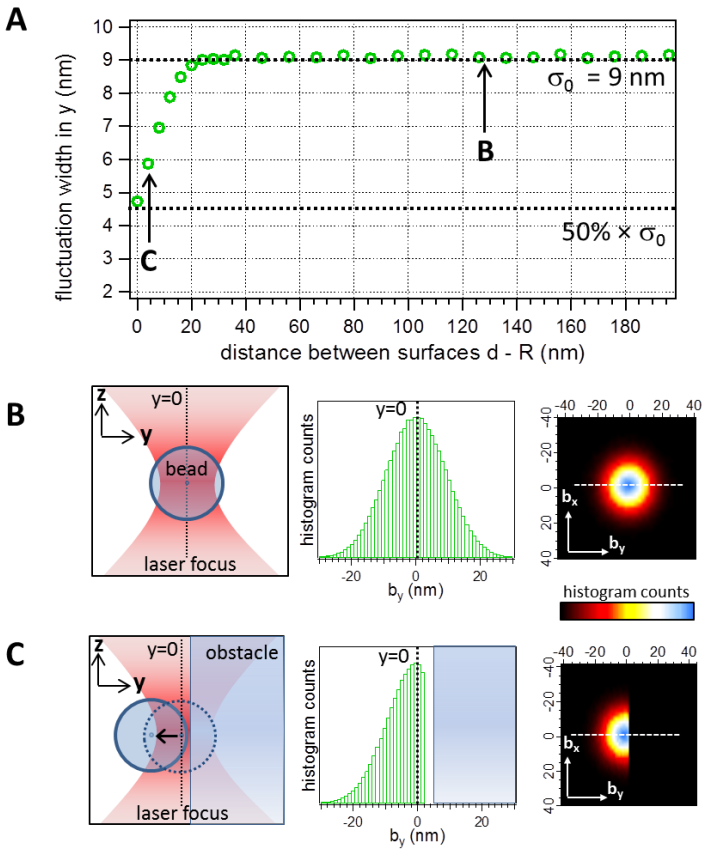

FIGURE S7 BD Simulation: (A) Distance-dependent fluctuation width $\sigma_y(d) = \sigma_\perp(d)$ of a $2R = 1$ µm bead's diffusive motion perpendicular to a rigid surface, calculated as the standard deviation of the fluctuation data. The histogram width $\sigma_\perp(d)$ decreases to 50% of its bulk value at $d = R$. (B) From left to right: Schematic illustration of the bead trapped by an undisturbed laser focus, histogram in y (perpendicular) direction along the white dotted line in the two-dimensional histogram (x-y-plane). (C) Illustration, one-dimensional and two-dimensional histograms for the case of an interface obstructing the bead's diffusive movement inside the optical trap.

Figure S7 *A* shows the distance-dependence of the histogram width perpendicular to an interface. An interface is successively brought closer to an optically trapped bead. As soon as the surface's distance to the trap center is smaller than one bead radius plus its fluctuation width, i.e., $d - R < \sigma_\perp$, the diffusive motion of the bead inside the optical trap is obstructed by the presence of the interface, as seen in Fig. S7 *C*. This results on the one hand in a shift of the bead's mean position $\langle b_y(t) \rangle$, which has been shown and discussed in the context of Fig. S4, and on the other hand in a decreasing fluctuation width σ_y as seen in Fig. S7 *C*, compared to the undisturbed case illustrated in Fig. S7 *B*. The simulation data show that the decrease at $d = R$, i.e., when the bead's surface and the obstacle's surface coincide, is $\sigma_y(d=R) = 50\% \times \sigma_0$, with σ_0 being the undisturbed histogram width in the absence of interfaces. This criterion has been used throughout this study to determine contact point of the bead and the cell membrane**.**

Results of alternative contact point analysis

As discussed in the main text, the membrane contact point cannot be precisely specified due to the optical influence of the pericellular matrix (PCM) on the fluctuation data. Two criteria to determine the contact point have been established and discussed, hereafter referred to as $\sigma_0/2$ and σ_{min} criterion, respectively. The alternative contact point obtained by the σ_{min} criterion is located in average (0.22 ± 0.09) µm behind the $\sigma_0/2$ contact point. The following Tables S1-S3 display the results of the fluctuation analysis, first by application of the $\sigma_0/2$ criterion (black numbers), then by application of the σ_{min} criterion (bold red numbers), for all cell types that were investigated.

TABLE S1 Comparison of hydrodynamic decay lengths Λ_j (mean values ± standard deviation) for various cell types depending on the choice of the membrane contact point criterion.

	J774	**MDCK**	**HT29**	
$\Lambda_\perp$	0.49 ± 0.03	0.65 ± 0.07	0.45 ± 0.03	(value at $\sigma_0/2$)
	0.43 ± 0.08 (-12%)	**0.57 ± 0.13** (-12%)	**0.40 ± 0.08** (-11%)	(value at σ_{min})
$\Lambda_{\parallel}$	0.27 ± 0.02	0.34 ± 0.02	0.28 ± 0.01	(value at $\sigma_0/2$)
	0.24 ± 0.06 (-11%)	**0.31 ± 0.05** (-9%)	**0.28 ± 0.05** (±0%)	(value at σ_{min})

TABLE S2 Comparison of maximum friction coefficient γ_{0j} (mean values ± standard deviation) for various cell types depending on the choice of the membrane contact point criterion.

	J774	**MDCK**	**HT29**	
$\gamma_{0\perp}$	5.11 ± 0.32	5.64 ± 0.28	6.23 ± 0.41	(value at $\sigma_0/2$)
	11.82 ± 0.84 (+131%)	**9.16 ± 0.55** (+62%)	**12.03 ± 0.94** (+93%)	(value at σ_{min})
$\gamma_{0\parallel}$	2.81 ± 0.59	2.83 ± 0.14	2.80 ± 0.27	(value at $\sigma_0/2$)
	3.92 ± 0.17 (+40%)	**4.62 ± 0.18** (+63%)	**4.47 ± 0.28** (+60%)	(value at σ_{min})

TABLE S3 Comparison of mean first passage times t_j for various cell types depending on the choice of the membrane contact point criterion.

	J774	**MDCK**	**HT29**	
$t_\perp$	0.340s (= 1.453×t_0)	0.384s (= 1.642×t_0)	0.326s (= 1.392×t_0)	(value at $\sigma_0/2$)
	0.745s (+119%) **(= 3.182×t_0)**	**0.827s** (+115%) **(= 3.354×t_0)**	**0.694s** (+113%) **(= 2.965×t_0)**	(value at σ_{min})
$t_{\parallel}$	0.259s (= 1.107×t_0)	0.277s (= 1.182×t_0)	0.262s (= 1.119×t_0)	(value at $\sigma_0/2$)
	0.281s (+8%) **(= 1.205×t_0)**	**0.341s** (+23%) **(= 1.457×t_0)**	**0.316s** (+21%) **(= 1.349×t_0)**	(value at σ_{min})

A graphical comparison of the results of Tables S1 – S3 is displayed in Figs. S8 – S10. It becomes obvious that the measurement of the hydrodynamic decay lengths are hardly influenced by the choice of the exact membrane contact point, see Fig. S8. A slight overall decrease of Λ_j in the range of 10% can be seen for all cell types. The maximum viscous drags $\gamma_{0\perp}$ and $\gamma_{0\parallel}$ exhibit a distinct increase of $\gamma_{0\perp}$ and $\gamma_{0\parallel}$, most pronounced in perpendicular direction, see Fig. S9. The change in γ_{0j} und Λ_j also affects the diffusion times t_j, which are significantly enlarged when the membrane is located further away from the 50% σ_0 point, see Fig. S10.

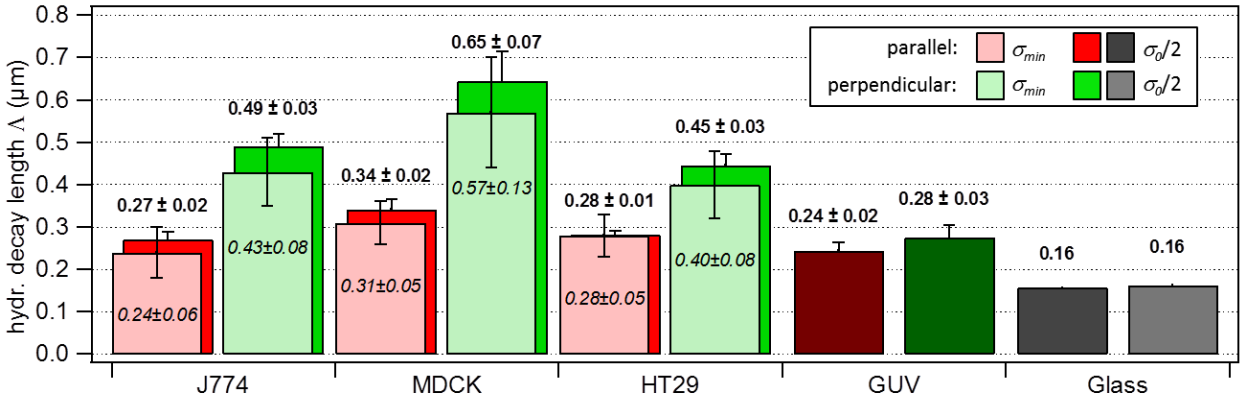

FIGURE S8 Hydrodynamic decay lengths $\Lambda_\perp$ and $\Lambda_\parallel$ for all cell types. The results obtained by the σ_{min} criterion are displayed in light red and green bars (mean values ± standard deviation in italics), bold numbers ± standard deviation and rich red/green bars correspond to membrane location estimated by $\sigma_0/2$.

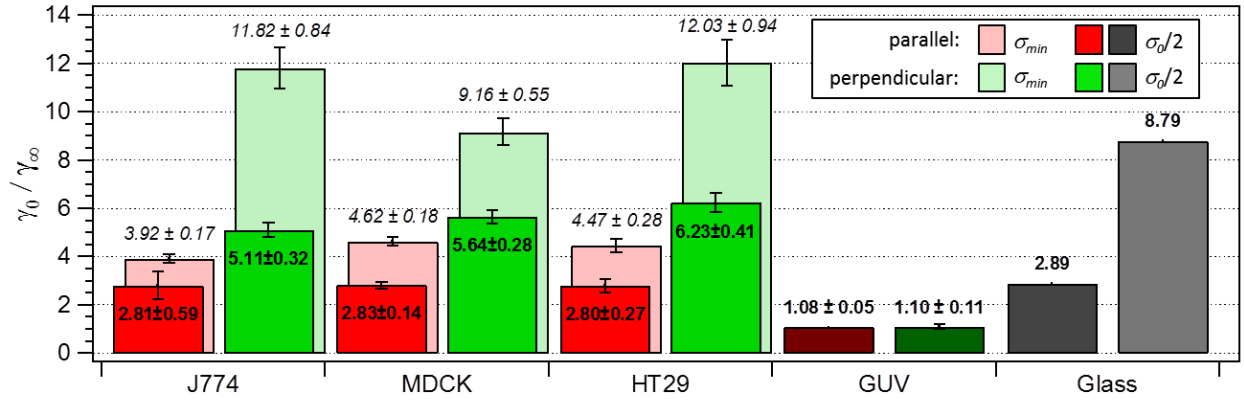

FIGURE S9 Maximum friction coefficient $\gamma_{0\perp}$ and $\gamma_{0|}$ for all cell types. The results obtained by the σ_{min} criterion are displayed in light red and green bars (mean values ± standard deviation in italics), bold numbers ± standard deviation and rich red/green bars correspond to membrane location estimated by $\sigma_0/2$.

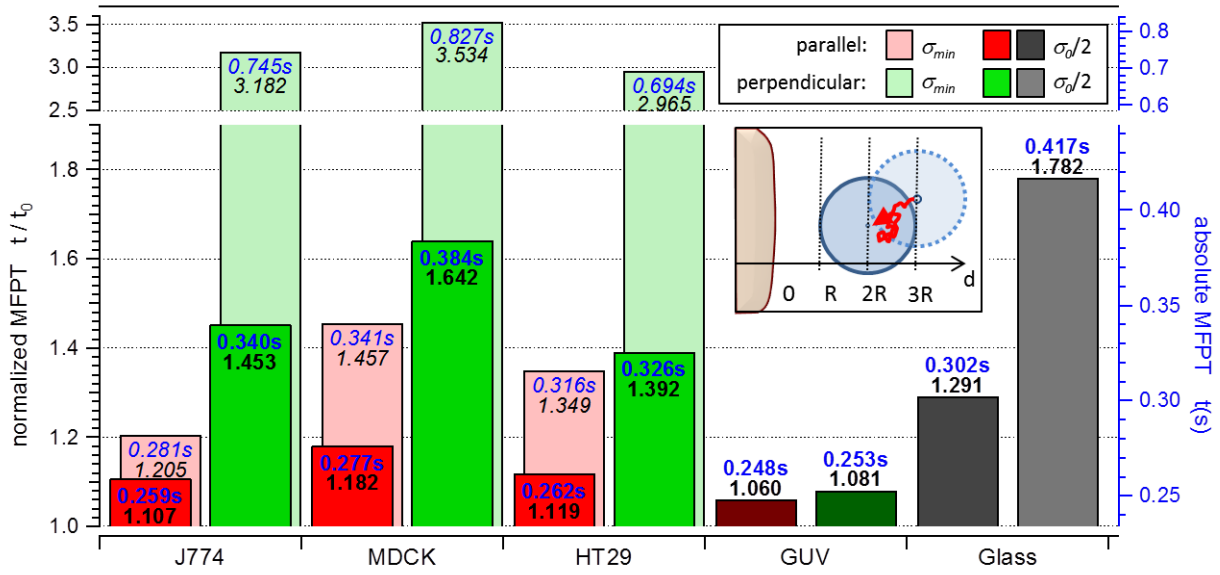

Figure S10 Mean first passage times $t_{0\perp}$ and $t_{0\parallel}$ for all cell types, considering the diffusion of a $2R$ = 1 µm sized bead from $d_1 = 3R$ toward $d_2 = 2R$. The results obtained by the σ_{min} criterion are displayed in light red and green bars (labels in italics), bold labels and rich red/green bars correspond to membrane location estimated by $\sigma_0/2$. Note the axis break between $1.9\times t_0$ and $2.5\times t_0$.

Data recording and fluctuation analysis of a bead approaching a glass interface

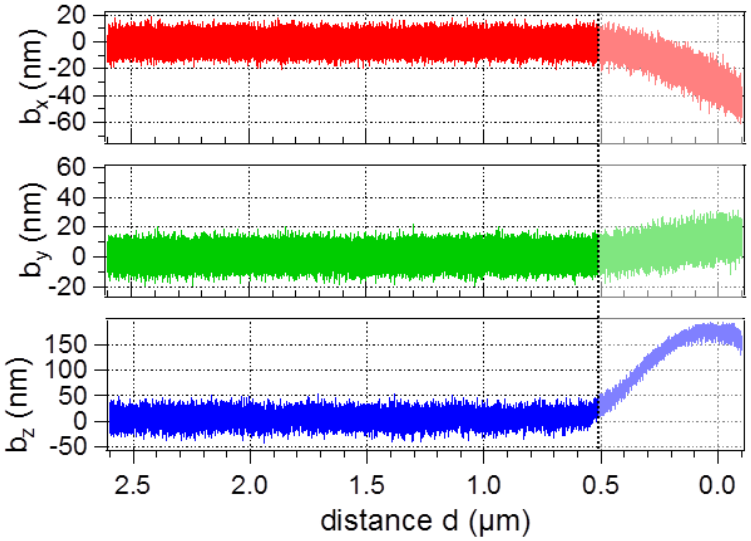

FIGURE S11 Fluctuation data of a 1 µm bead approaching a stiff glass coverslip in *z* direction. Distance-dependent position trajectories $b_x(d,t)$, $b_y(d,t)$, $b_z(d,t)$ calculated from the QPD data after calibration. *z* data correspond to scan direction. Contact between bead and coverslip at $d = R$ is indicated by the black dotted line and the shaded region at $d \leq R$.

The experiments with glass coverslips as obstructing interfaces were performed under slightly different geometrical and experimental conditions. In contrast to the cell experiments, where the surface was approached in lateral (*y*) direction, the glass coverslip was approached in -*z* direction, i.e., in reverse propagation direction of the laser light. The scan was performed over a *z* range of 5 µm, of which roughly 2.5 µm are shown in Fig. S11, with Δz = 20 nm steps as in the cell experiments. To account for the intrinsically weaker trap stiffness in *z* direction compared to *x* and *y*, the laser power was increased to 60 mW compared to 40 mW in cell experiments. This results in increased overall trap stiffnesses compared to the cell experiments, as seen in Fig. S12. Figure S11 displays the distance-dependent fluctuation data calculated from QPD signals via calibration upon approaching the glass coverslip with an optically trapped 1 µm bead. Blue data points (*z* data) correspond to scan direction. The mean signal shift, noticeable already at distances of roughly 1 µm before contact in all cell experiments, is not observed in this experiment due to the different geometrical circumstances: Whereas the cell is placed only at one side of the optical trap, thus asymmetrically scattering the laser light and leading to a shift of the mean signal due to destructive interferences, the glass coverslip is practically infinitely extending to both sides of the laser focus, thus having no optical effect on the QPD signals. The narrowing of the fluctuation data in scan direction becomes apparent as d approaches $d = R$ (contact between bead and coverslip).

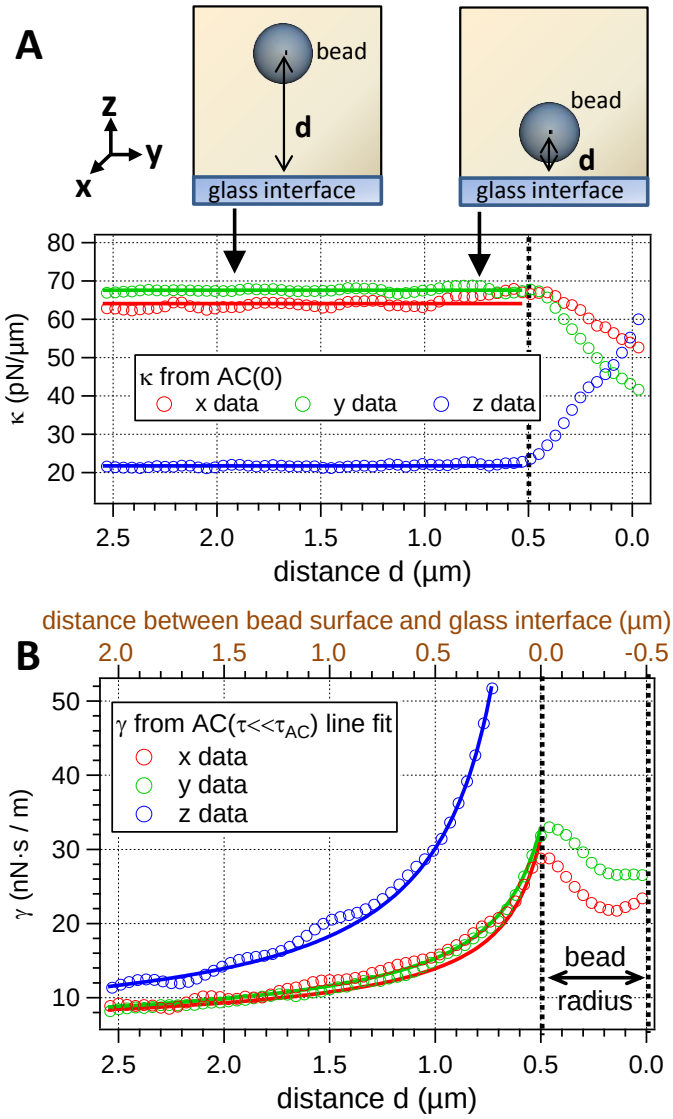

FIGURE S12 The bead's distance d to the glass coverslip is subsequently decreased in z direction (blue data), as illustrated in the schematic sketch. Contact between the bead surface and coverslip is marked by a vertical dotted black line at d = 0.5 µm. (A) The stiffness parameter $\kappa_j(d)$ and (B) the viscous drag $\gamma_j(d)$ are plotted as a function of d. Solid lines indicate fits to the data points according to Happel's & Brenner's formula.

Figure S12 shows that all components κ_j (j = x,y,z) of the stiffness parameter remain constant until mechanical contact between the bead and the coverslip is established, as indicated by additional line fits. The friction coefficients $\gamma_j(d)$ increase as the bead approaches the interface. The increase of the friction component perpendicular to the glass coverslip, i.e., $\gamma_z(d)$ displayed in blue, is significantly higher than $\gamma_x(d)$ and $\gamma_y(d)$ in parallel direction (red and green circles). Happel's and Brenner's formula allows to quantify the distance-dependent behavior of $\gamma_j(d)$ close to a stiff, infinitely large flat interface and was fitted to the data points. Measurement and fit results are in excellent agreement.

Data recording and fluctuation analysis of a bead approaching a GUV

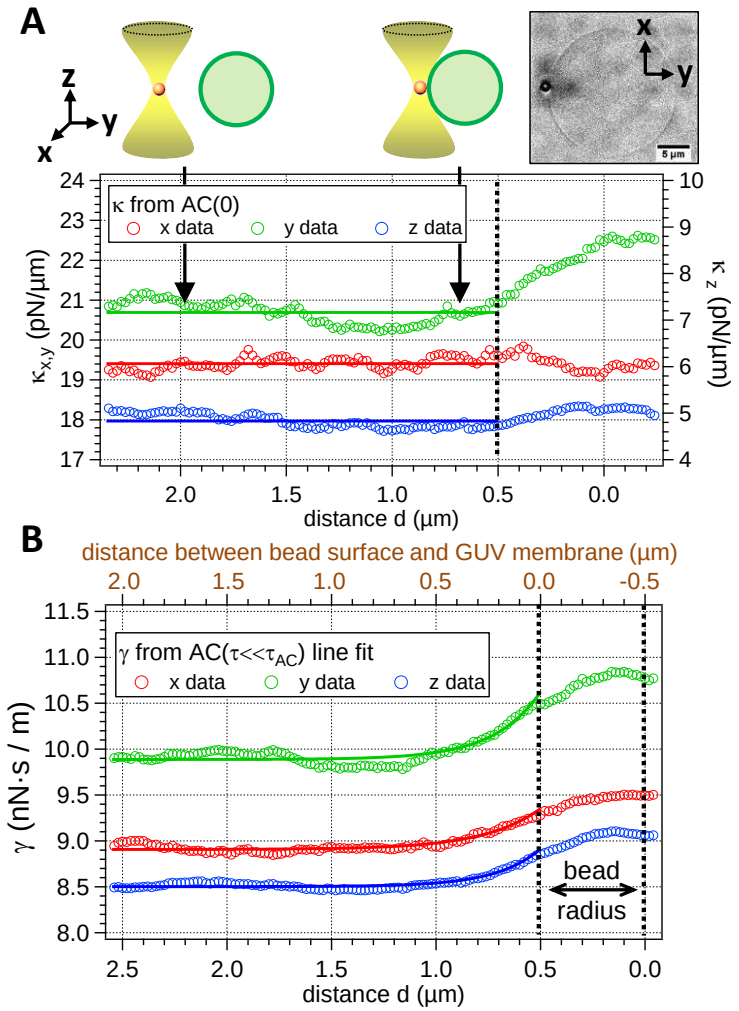

FIGURE S13 Distance-dependent stiffness and viscous drag of a 1 µm bead approaching a GUV. The bead's distance d to the GUV membrane is subsequently reduced in y direction (green data), as illustrated in the schematic sketch. Contact between the bead surface and membrane is marked by a vertical dotted black line at d = 0.5 µm. (A) The stiffness parameter $\kappa_j(d)$ and (B) the viscous drag $\gamma_j(d)$ are plotted as a function of d. Solid lines indicate fits to the data points.

The distance-dependent stiffness and viscous drag upon approaching a GUV membrane are displayed in Fig. S13. Again, a constant $\kappa_j(d)$ can be seen at $d \geq R$, while at the same time $\gamma_j(d)$ increases exponentially. The overall increase in $\gamma_j(d)$ is much smaller than in the cell experiments, regardless of the spatial dimension $j = x,y,z$ and no anisotropic behavior of the hydrodynamic decay length is observed. These results are discussed in detail in the main text. Due to the weaker laser power in the GUV experiment, the overall stiffnesses $\kappa_j(d)$ are smaller than in the cell experiments. However, as the viscous drag $\gamma_j(d)$ is independent of the choice of experimental parameters like laser power, results for $\gamma_j(d)$ are comparable with those obtained from cell experiments.

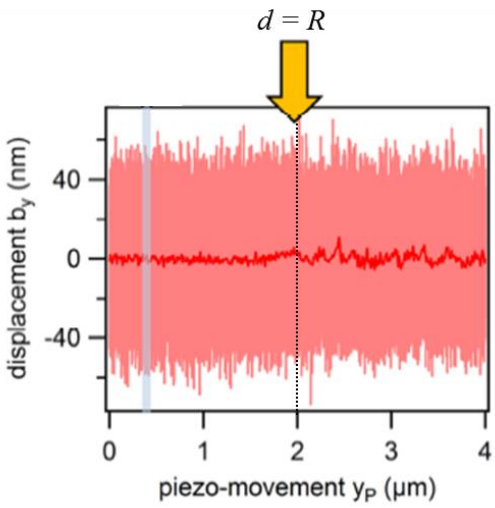

FIGURE S14 Bead displacement $b_y(d)$ upon approaching a GUV membrane. Light red data show the bead's trajectory in scan direction while the piezo stage (coordinate y_p) was successively moved towards the GUV membrane. The dark red curve shows the smoothed trajectory. Contact between bead surface and membrane of the unfixed GUV at $d=R$, corresponding to y_p = 2 µm in this experiment, is indicated by the dotted black line and the yellow arrow. Illustration was taken from (3) with the author's permission.

Figure S14 shows the calibrated bead's trajectory in scan direction upon approaching the membrane of an unfixed GUV. After contact, the 20 µm large GUV is dragged to the side by the moving bead. The method to determine the contact point $d = R$ is described in (3) and shall not be explained here.

Frequency-dependence of the viscous drag

In general, the viscosity in direction $j = \perp,\parallel$ is frequency-dependent. Fourier transformation of the overdamped Langevin (Eq. 1 in the main text) yields:

$$\tilde{b}_j(\omega)\cdot\left(i\omega\cdot\tilde{\gamma}_j(\omega,d)+\kappa_{opt,j}-\tilde{\kappa}_{cell,j}(\omega,d)\right)=\tilde{F}_{th,j}(\omega) \tag{S3}$$

As long as no binding to the membrane or to cellular protrusions occurs, the system consisting of bead and surrounding fluid is in thermal equilibrium. Thus, the fluctuation-dissipation-theorem and the Kramers-Kronig relations can be applied to extract the storage and loss moduli $G'(\omega)$ and $G''(\omega)$ from the fluctuation data (2). In this case, the loss modulus $G''(\omega)=1/6\pi R\cdot\omega\cdot\tilde{\gamma}(\omega)$ increases with the frequency-dependent drag coefficient $\tilde{\gamma}(\omega)$, but amplifies higher frequencies by the multiplication with ω. Details of the calculation procedure can be found in (4, 5).

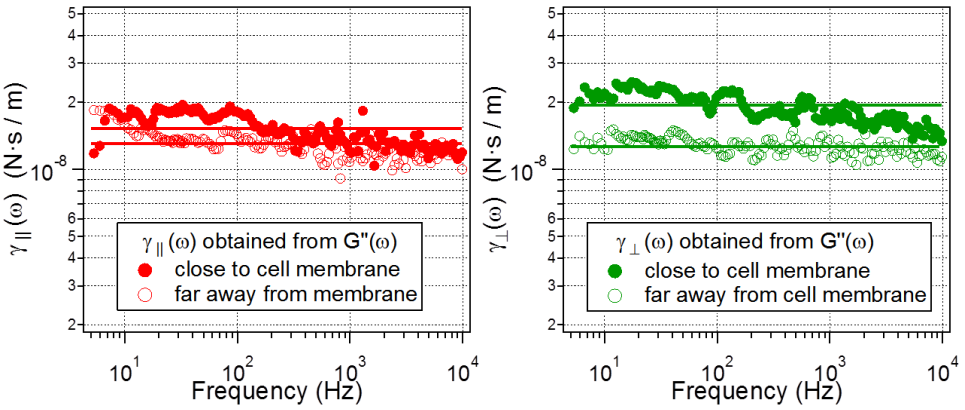

FIGURE S15 Frequency-resolved viscous drag $\gamma_j(\omega)$ ($j = \perp,\parallel$) for two different distances to the membrane of a MDCK cell. Hollow circles denote data recorded far away from the membrane (d-$R >> \Lambda$), full circles represent a distance of approximately d-R = 0.3 µm. The solid lines indicate fits to the data points.

Figure S15 displays the frequency-dependent viscous drag $\tilde{\gamma}(\omega)$ for two different distances d between bead and cell. Here, hollow circles represent a distance $d-R \gg \Lambda_{\parallel,\perp}$ much larger than the measured hydrodynamic decay length and solid circles represent a small distance $d-R=0.3\,\mu\text{m}<\Lambda_{\parallel,\perp}$. Red and green colors denote parallel and perpendicular particle motions, respectively. It is apparent from Fig. S15 that $\tilde{\gamma}(\omega)$ remains approximately constant over the whole frequency range under investigation ($\omega/2\pi \leq 10$ kHz), both for parallel and perpendicular data. Nearby the cell membrane, the mean value $\gamma_\parallel(\omega)$ increases only modestly by 18%, whereas the mean $\gamma_\perp(\omega)$ increases by 51%. Again, it can be seen that the rise of the mean value of $\gamma_\perp$ for short particle-cell distances is higher than the rise of the mean $\gamma_\parallel$. The slow drop-off at high frequencies is ascribed to numerical artifacts during calculation, resulting from a finite upper frequency limit (6). Also, reliable results are only obtained up to a maximum frequency of about 10 kHz due to the finite maximum frequency. The results exemplarily presented in this chapter agree with $\gamma_\perp$ and $\gamma_\parallel$ obtained from the procedure described in Eq. 2 and presented in Fig. 6 in the main text. Furthermore, it can be seen that $\gamma_j(d)$ has no frequency-dependent contribution and that averaging over all frequencies ω is justified.

Visco-elastic analysis of the fluctuation data via passive microrheology

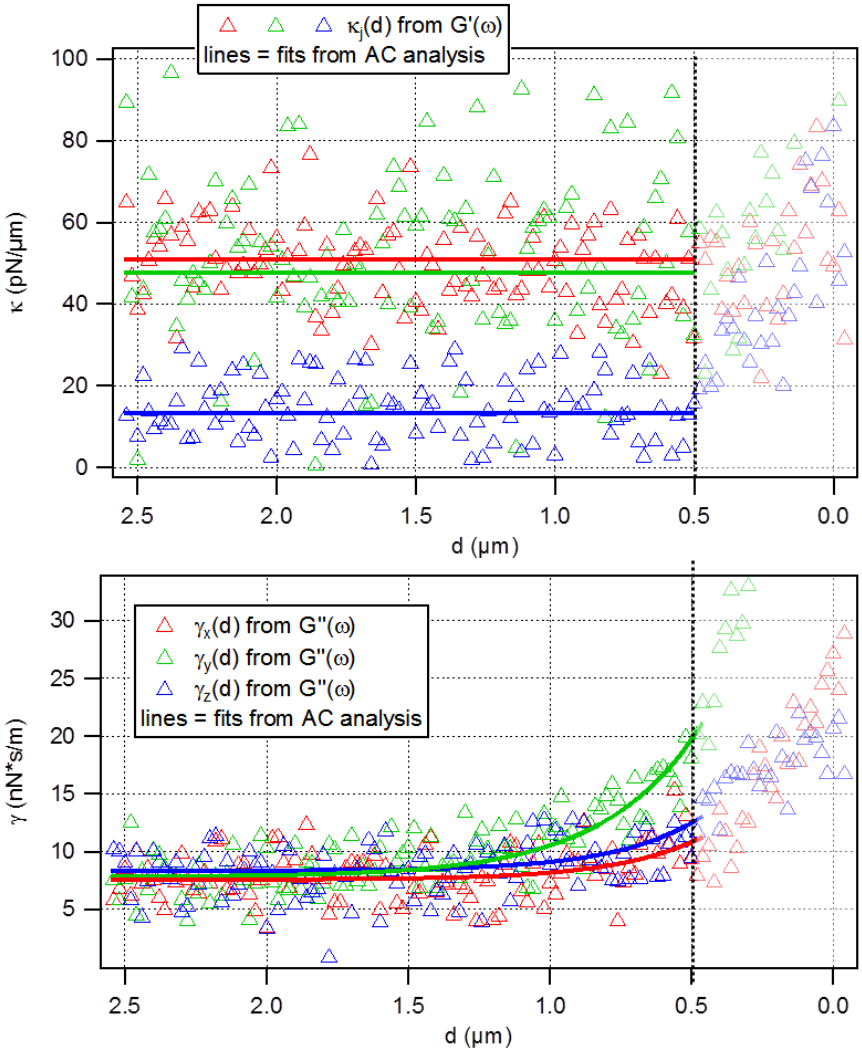

FIGURE S16 Analysis of the fluctuation data of a 1 µm bead approaching a HT29 cell membrane via passive microrheology. (A) The distance-dependent stiffness parameter $\kappa_j(d)$ was calculated from the real part of the complex shear modulus, $G'(\omega) = Re(G(\omega))$. (B) The imaginary part $Im(G(\omega)) = G''(\omega)$ was used to calculate the viscous drag $\gamma_j(d)$.

The fluctuation data that was shown in Fig. 4 in the main text was analyzed with the help of the microrheology toolbox, that has been shortly introduced in the previous paragraph and, e.g., in (4, 5).

In brief, the linearized response function $\alpha(\omega)$ of a spherical particle with radius R displaced by $\tilde{b}(\omega)$ reacts to a driving force such that $\tilde{b}(\omega) = \alpha(\omega) \cdot \tilde{F}(\omega)$. $\alpha(\omega)$ is inversely proportional to

the complex shear modulus $G(\omega) = (6\pi R \cdot \alpha(\omega))^{-1}$. For a thermal driving force $\tilde{F}_{th,j}(\omega)$ it follows from Eq. S3 that

$$\alpha_j(\omega) = \frac{\tilde{b}_j(\omega)}{\tilde{F}_{th,j}(\omega)} = \frac{1}{i\omega \cdot \tilde{\gamma}_j(\omega,d) + \kappa_{opt,j} - \tilde{\kappa}_{cell,j}(\omega,d)} \ , \tag{S4}$$

resulting in the complex shear modulus

$$G_j(\omega) = \frac{\kappa_{opt,j} - \tilde{\kappa}_{cell,j}(\omega,d) + i\omega \cdot \tilde{\gamma}_j(\omega,d)}{6\pi R} \tag{S5}$$

with real and imaginary parts

$$G_j'(\omega) = \frac{\kappa_{opt,j} - \tilde{\kappa}_{cell,j}(\omega,d)}{6\pi R} \qquad \text{and} \qquad G_j''(\omega) = \frac{\tilde{\gamma}_j(\omega,d) \cdot \omega}{6\pi R} . \tag{S6}$$

Eq. S6 shows that the real part (accounting for elastic components) and the imaginary part (viscous component) of the complex shear modulus are independent of each other. Therefore, the increase in $\kappa_y(d)$ on the last 0,2 µm before contact, as seen in Fig. 4, does not lead to a miscalculation of $\gamma(d)$. This increase is probably due to transient binding to the glycocalyx surrounding the cell membrane.

Figure S16 shows the stiffness $\kappa_j(d)$ and viscous drag $\gamma_j(d)$ of the very same data presented in Fig. 4, calculated by Eqs. S4-S6. The resulting noise is inherent to passive microrheological data analysis via Kramers-Kronig transform. Nevertheless, the rather constant behavior of $\kappa_j(d)$ ($j=x,y,z$) can be observed, as indicated by the line fits from Fig. 4. Also, the smooth increase in $\gamma_j(d)$ can still be seen in Fig. S16, visualized by least-square fits which reveal the same result as those plotted in Fig. 4.

In conclusion, we have shown that the transient binding, be it to the glycocalyx or to any other structure surrounding the cell membrane, does not corrupt the correct measurement of $\gamma_j(d)$. Figure S16 confirms the theoretical concept presented above despite the relatively strong scattering of the data points.

SUPPORTING REFERENCES

1. Grassia, P. S., E. J. Hinch, and L. C. Nitsche. 1995. Computer Simulations of Brownian Motion of Complex Systems. J. Fluid Mech. 282:373-403.
2. Landau, L. D., and E. M. Lifshitz. 1969. Statistical Physics. Pergamon Press, Oxford, UK.
3. Meinel, A., B. Tränkle, W. Römer, and A. Rohrbach. 2014. Induced phagocytic particle uptake into a giant unilamellar vesicle. Soft Matter 10 3667 - 3678.
4. Buchanan, M., M. Atakhorrami, J. F. Palierne, F. C. MacKintosh, and C. F. Schmidt. 2005. High-frequency microrheology of wormlike micelles. Phys. Rev. E 72:011504.
5. Gittes, F., B. Schnurr, P. D. Olmsted, F. C. MacKintosh, and C. F. Schmidt. 1997. Microscopic viscoelasticity: Shear moduli of soft materials determined from thermal fluctuations. Phys. Rev. Lett. 79:3286-3289.
6. Schnurr, B., F. Gittes, F. C. MacKintosh, and C. F. Schmidt. 1997. Determining microscopic viscoelasticity in flexible and semiflexible polymer networks from thermal fluctuations. Macromolecules 30:7781-7792.